Soft Matter

www.rsc.org/softmatter

Volume 8 | Number 13 | 7 April 2012 | Pages 3499–3706

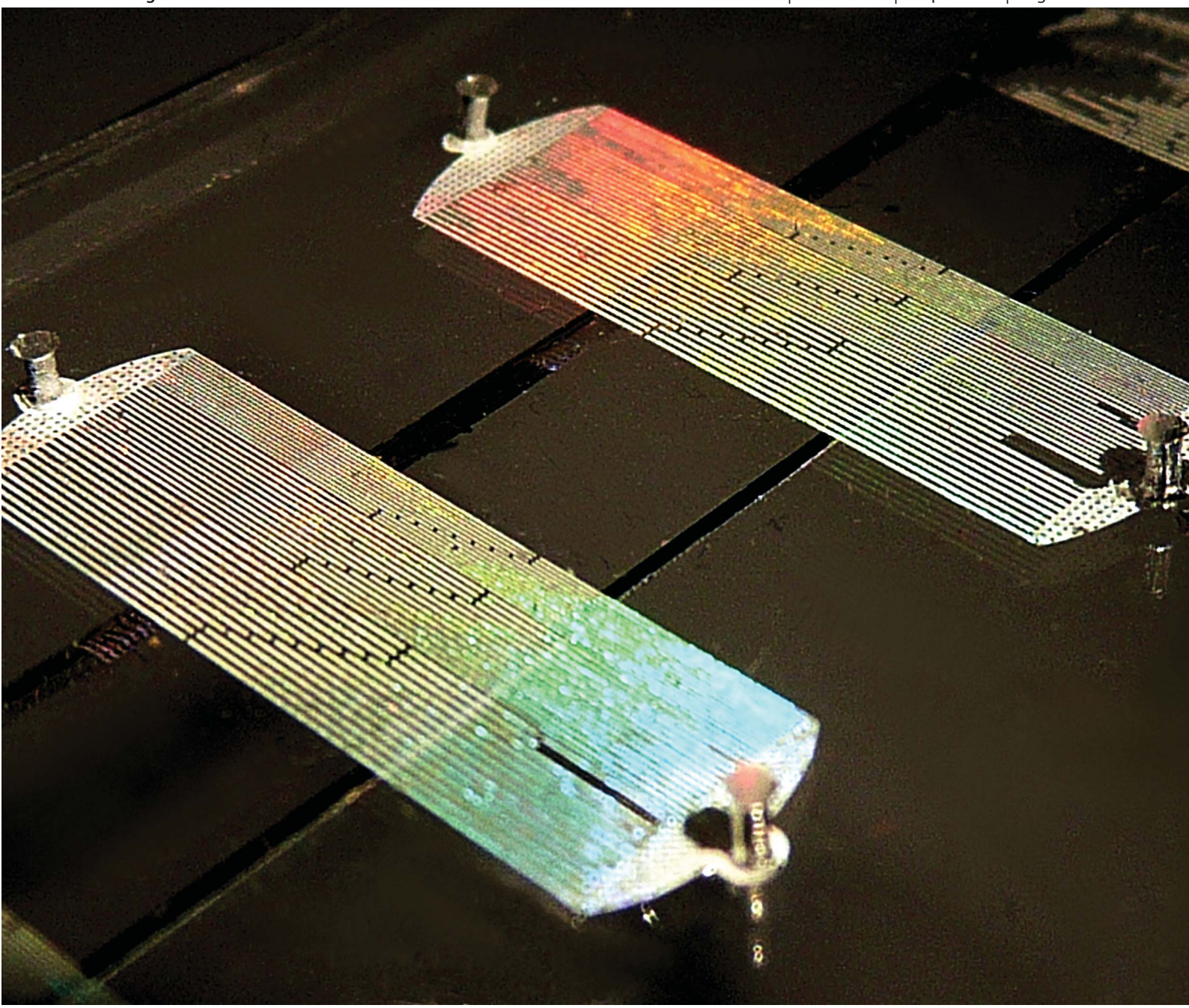

ISSN 1744-683X

RSC Publishing

PAPER

Jacques Leng *et al.*

Microfluidic-assisted growth of colloidal crystals

1744-683X(2012)8:13;1-E

Soft Matter

Dynamic Article Links

Cite this: *Soft Matter*, 2012, **8**, 3526

www.rsc.org/softmatter

PAPER

Microfluidic-assisted growth of colloidal crystals†

Aurore Merlin, Jean-Baptiste Salmon and Jacques Leng*

Received 10th November 2011, Accepted 4th January 2012
DOI: 10.1039/c2sm07149e

We investigate the concentration process of dilute dispersions of charge-stabilized colloids using a dedicated microfluidic tool based on evaporation. We observe the nucleation and growth of colloidal crystals with typical dimensions of $10 \times 50\ \mu m^2 \times$ several millimetres whose growth kinetics and structures are characterized using optical, confocal, and electron microscopy. We demonstrate with systematic screening experiments that microfluidics yields a precise control on the growth pace of these dense organized colloidal states. We then predict the growth rate of these colloidal structures with a model of the suspension (hard-spheres) that accounts for a diverging collective diffusion coefficient near the close-packing; this description helps us understand why the kinetics can be anticipated on the basis of a simple conservation law. Finally, our experiments unveil the important role played by ions which are also present in the initial dilute dispersion and therefore also get concentrated simultaneously with colloids, and their influence on the ordering.

1. Introduction

Guiding the assembly of colloids is an active field of research which is driven both by the intrinsic aesthetics of these model systems and by the applications promised by well-organized colloidal structures: photonics, sensing, catalysis, metamaterials, *etc.*[1,2] Such a bottom-up approach required the development of ingenious techniques to concentrate dilute dispersions containing the colloidal nano- to micro-structures (10–1000 nm) up to the formation of three-dimensional organized assemblies: successive dip-coatings[3] or evaporation-induced self-assembly,[4–6] simple sedimentation[7] or the use of patterned surfaces,[8] filtration,[9,10] and drying in many geometries (sessile droplets,[11] films,[12] spherical droplets,[13] or of dispersions confined in tubes,[14,15] see also the following reviews[16,17]) have all been widely used. In most of these methods, a high concentration of colloids is reached locally (*e.g.*, close to the contact line of a sessile droplet) thanks to the interplay of evaporation and convection and sometimes also capillarity, which leads to the formation of organized colloidal structures.

The above mentioned techniques have often been successful at forming spectacularly well-organized colloidal crystals but investigations of the exact mechanisms at work are not so frequently addressed in the literature. Transport phenomena leading to the local increase of the concentration of the dispersion have been well-understood in the case of evaporation-induced self-assembly,[18] sedimentation,[19] evaporation from droplets,[20] and uni-directional solidification,[21,22] but a complete understanding is still a major challenge. Indeed, these methods explore complex out-of-equilibrium routes from dilute dispersions up to dense organized colloidal crystals through nucleation and growth steps, that also often involve important solvent flows[23,24] and/or specific interactions.[25]

In the present paper, we use a microfluidic chip, referred below to as a microevaporator, to build colloidal crystals in confined microchannels at a controlled pace. Microevaporators permit the concentration of any aqueous solution or dispersion by the mean of solvent extraction.[26–28] The principle consists in using a semi-permeable membrane across which water can permeate and escape from a microchannel containing the solution or dispersion of interest (Fig. 1). Because the solute does not evaporate, it gets concentrated at the tip of the microcapillary. Such devices were demonstrated to be successful at concentrating electrolyte solutions,[28] surfactants,[29] polymers,[30] or even nanoparticles[31] up to dense states, such as crystals, mesophases, gels, *etc.* in a controlled way. These tools provide original and well-defined out-of-equilibrium routes through a phase diagram from dilute up to dense states and we will later give a brief overview on the operational parameters that permit tuning of the concentration kinetics.

We used this microevaporation technique to concentrate colloidal dispersions up to the nucleation and growth of dense colloidal structures. Using a pseudo hard-sphere model system, we demonstrate that our method can produce millimetre-long

Univ. Bordeaux/CNRS/RHODIA, LOF, UMR 5258, 178, Avenue Schweitzer, F-33600 Pessac, France. E-mail: jacques.leng-exterieur@eu.rhodia.com; Fax: +33556464790; Tel: +33556464749

† Electronic supplementary information (ESI) available: We provide four movies and an additional figure; Movie 1 shows the nucleation and growth of a colloidal crystal (related to Fig. 4), Movies 2 and 3 are related to Fig. 9 and show confocal movies obtained from ordered and disordered growing structures, Fig. S1 illustrates the difference of structure *via* the pair correlation function of the two structures, and Movie 4 shows the dissolution kinetics (related to Fig. 10). See DOI: 10.1039/c2sm07149e

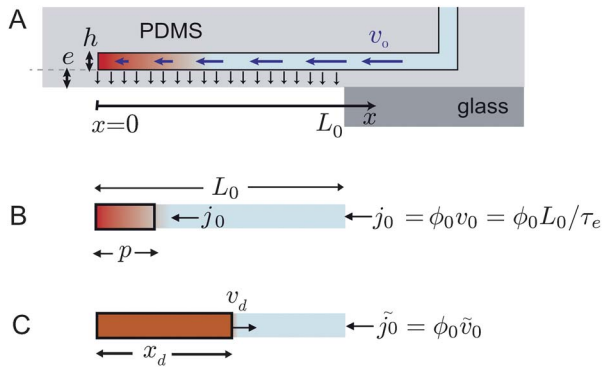

Fig. 1 (A) Side view of a microevaporator showing the dead-end channel of thickness h, (width w), and length L_0, connected to a reservoir, and in contact with a membrane of thickness e. The color gradient mimics the concentration gradient of a solute that results from the solvent flow across the membrane (blue arrows). A glass slide covers a part of the membrane to define the permeation zone. (B) Extreme simplification of the mechanisms at work: the evaporation zone of length L_0 serves as a suction pump which drives solvent and solute toward the tip of the evaporator; the solute that does not evaporate gets accumulated into a box of a size $p = (D\tau_e)^{1/2}$. (C) Growth of a dense state (red) in the microevaporator at a velocity v_d. The incoming flux of solute $\tilde{j_0}$ may differ from $\phi_0 v_0$ when the dense state modifies the evaporation rate.

colloidal crystals confined in microchannels with typical transverse dimensions $\approx 10 \times 50$ μm^2. Importantly, the microfluidic format yields a precise control on the growth pace of the colloidal crystals as well-demonstrated by a combination of two results: first, we can tune the growth kinetics of crystalline fronts with operational parameters of the microevaporator; then, we are able to predict this growth rate with simple models of the suspension. Eventually, local views of the dense colloidal assemblies combined with structural measurements reveal the crucial role played by the electrostatic interactions, and therefore by the ionic strength, on the ordering (or not) of the suspension.

Indeed, as for other similar techniques (drying of droplets, unidirectional solidification…), microevaporation concentrates all the chemical species, including colloids and ions, and we observe that the decrease of the electrostatic interactions due to the concentration of the ionic species has a dramatic influence on the self-assembly process.

2. Material and methods

2.1 Colloidal suspension

The colloidal system we investigated is a latex suspension of polystyrene (PS) beads in water (Microspheres from Invitrogen). The nominal radius is $R_p = 250$ nm (nominal size polydispersity 2%) and the mass fraction of solid 8%. The beads bear a sulfate surface charge to ensure colloidal stability; the dispersion also contains 2 mM of sodium azide as a preservative‡. For some specific experiments, we also used fluorescent yellow-green polystyrene microspheres of the same size, from the same supplier, dyed with a fluorophore which emits around 520 nm. For the volume fraction conversion, we use the density of bulk polystyrene $\rho_{PS} = 1.05\ 10^3$ kg m^{-3} whichever stock dispersions we use. The refractive index of PS is $n \approx 1.59$.

We then prepare dilutions of this stock dispersion by adding a desired amount of deionised water (Millipore, resistivity 18.2 MΩ/cm) after a careful and required cleansing of all the vials (*e.g.*, non sterile polypropylene vials) in order to suppress the possible pollution by ionic soluble species. The dispersions we finally utilize have a typical volume fraction ϕ_0 between 0.1 and 4%.

‡ According to the supplier, "the microsphere suspensions are stable at up to about 0.2 M univalent electrolyte concentrations, but will readily agglomerate in the presence of low concentrations of divalent cations unless stabilized by a hydrophilic coating", which is not the case.

2.2 Microevaporation

2.2.1 Basics of microevaporation

2.2.1.1 Evaporation-induced pumping. A microchannel of width w, height h, and length L_0 is exposed by construction to a thin poly(dimethylsiloxane) (PDMS) membrane of thickness e (Fig. 1A). Typical dimensions are $h = 5$–30 μm, $w = 20$–100 μm, $L_0 = 0.5$–10 mm, and $e = 10$–30 μm. The channel is filled with a solution (or a dispersion) and connected to a reservoir with a large volume (>10 μL). The membrane which is permeable to water only is exposed on the dry side to a stream of dehydrated air at room temperature.

Because of the contrast of chemical potential of water between the channel compartment [$\mu_w(\phi)$ with ϕ the concentration of solute] and the dry side [$\mu_w^{gas} < \mu_w(\phi)$], the water permeates across the membrane of surface wL_0. It yields a water loss in the channel at a rate $L_0 w v_e$ (m^3 s^{-1}) which induces a net replacement flow from the reservoir. There is therefore an incoming velocity at the entrance of the evaporation zone $v_0 = (L_0 w v_e)/wh = v_e(L_0/h)$. Estimates of v_e based on Fick-diffusion across PDMS membranes ($e = 10$–30 μm) are only $v_e \sim 10$–50 nm s^{-1}. However, the microfluidic format amplifies considerably the evaporation-induced flow, by the geometrical factor $L_0/h = 10^2$–10^3. Evaporation across the membrane also casts a typical timescale on the process $\tau_e \equiv L_0/v_0 = h/v_e$, the time needed to empty one volume of channel whL_0 ($\tau_e \approx 10^2$–10^3 s).

2.2.1.2 Evaporation-induced concentration. The concentration of the solute occurs as a consequence of this evaporation-induced flow. Indeed, when the reservoir contains a solute at a volume fraction ϕ_0 (non permeable in PDMS), the latter enters the evaporation zone with a flux $j_0 = \phi_0 v_0$, and is driven toward the tip of the capillary where it accumulates. For solutes that do not alter the evaporation rate (*i.e.*, $\mu_w(\phi) \approx$ cste), the evaporation-induced velocity profile is linear in the evaporation zone, $v(x) \propto x$. Convection [flux $j_c = \phi(x)v(x)$] and diffusion ($j_d = -D\partial\phi/\partial x$, D is the diffusion coefficient of the solute) compete together, yet due to the linear velocity profile, it is possible to separate the space into two distinct regions with a crossover at a distance $p = \sqrt{D\tau_e}$ defined by the balance of the two fluxes $j_d \sim j_c$. For $x \gg p$, convection dominates while diffusion dominates for $x \ll p$ (Fig. 1B).

The accumulation rate of solute in the diffusion-dominated zone (volume $\approx pwh$) is estimated by solute conservation: the convection-dominated zone serves essentially as a pump which delivers solute at a rate $(wh)j_0$ which induces a concentration increase:

$$\frac{d\phi}{dt} \approx \frac{(wh)j_0}{pwh} = \frac{v_0\phi_0}{p} = \frac{L_0}{p}\frac{\phi_0}{\tau_e}. \quad (1)$$

This estimate shows that several tunable factors directly affect the concentration rate: the length L_0 of the pump; the concentration in the reservoir ϕ_0; the evaporation time τ_e which in turn depends on the geometry ($\tau_e = h/v_e$); the accumulation zone which depends both on the geometry *via* τ_e and on the solute *via* D.

2.2.1.3 Concentration up to the growth of dense states. The evaporation-induced concentration holds up to high concentrations of solutes, for which the naive picture outlined above is not valid anymore. In that case, experiments[28–31] show that in most of cases, a dense state forms at the tip of the microevaporator, and grows continuously (Fig. 1C). Schindler and Ajdari[35] produced a complete theoretical picture describing such a scenario, which will be recalled later in the text. We only discuss simply here two limiting cases.

(i) The first one concerns molecular mixtures (salt, polymers…) for which evaporation stops at $\phi \approx \phi_d$ due to the decrease of the chemical potential of water $\mu_w(\phi)$ (*e.g.*, a crystal that nucleates in a supersaturated solution). In that case, a dense state at $\phi \approx \phi_d$ grows at a velocity v_d in the microevaporation zone. The length of the pump is consequently reduced (Fig. 1C), and the growth velocity v_d decreases as the dense state invades the microevaporator, as observed for several systems (crystals,[28] dense mesophases of surfactants[29]).

(ii) The second limiting case concerns colloidal dispersions for which a dense state may also grow at a velocity v_d, as demonstrated later in the present work. This growth is not due to a decrease of the evaporation rate (water still flows through the pores of a dense colloidal packing), but because of the incompressibility of the colloidal dispersion when approaching the close-packing fraction $\phi \to \phi_d$ (see Sec. 4). In this scenario, one naively expects that the incoming flux of colloids $\phi_0 v_0$ is unchanged, and that the growth rate of the colloidal dense state follows $\phi_d v_d \approx \phi_0 v_0$ (for $\phi_0 \ll \phi_d$, see Sec. 3). Simple measurements of the growth rate v_d may thus give a quantitative estimate of the density of the colloidal dense packing ϕ_d, as shown later on the experimental system studied here.

2.2.2 Screening chip. We use the estimate of eqn (1) to guide the fabrication of a chip which allows the screening of many different concentration conditions in a single experiment. The basic element is a microevaporation channel as described before (Fig. 1); the typical dimensions are w = 50–100 μm, height h in the range 10–30 μm, length L_0 in the range 1–5mm. A chip consists of a group of 9 parallel of the microevaporation channels, all of different length L_0, which are all connected to the same reservoir (Fig. 2). Additionally, we position 2 extra channels on both sides of the group that will prevent side effects, *i.e.*, the fact that a channel with no neighbor evaporates differently.[32] Also, we position two of these groups in front of each other in order to double the number of possible experiments and optimize symmetry (Fig. 2). Eventually, the final chip comprises four of these doubled groups of microevaporation screening devices, from which we expect $4 \times 2 \times 9 = 72$ possible measurements.

All structures were created using standard soft photolithography techniques.[33] A master template is made with a photocurable resist which is then moulded in PDMS and cured at high temperature. This elastomeric core is peeled off the template and punched to create an opening for the reservoir, either a polyethylene tubing or simply a large opening of 4 mm diameter; the body of the chip is then sealed with a thin PDMS membrane of thickness $e \approx$ 10–20 μm and either the gradient technique[34] or plasma activation is used to firmly bind the two elements. We use microscope slides to cover specific areas of the membrane where we want to suppress permeation, and thus define the length L_0.

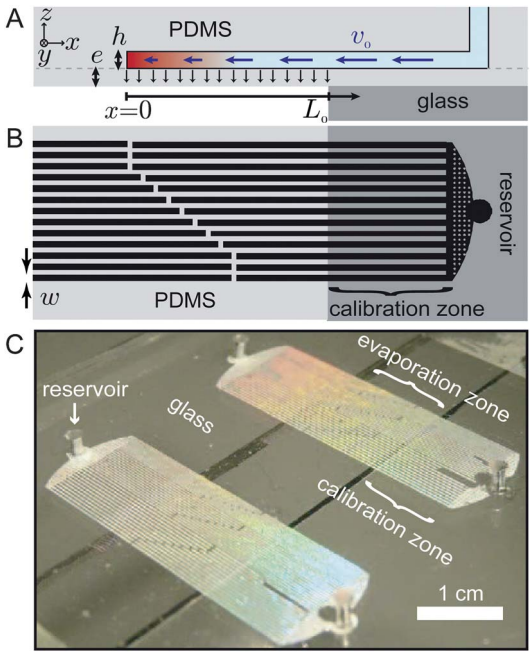

Fig. 2 (A) Side view of a microevaporator showing its dimensions and axes. (B) Top view of the screening geometry with 9 channels of different lengths all connected to the same reservoir. Two of these microsystems face each other in order to increase the number of tests. (C) Picture showing 2 × 2 of the 8 microsystems fabricated in one microchip. The microsystems are filled with colloidal crystals that Bragg-diffract the light when shone with a diffuse white light.

2.2.3 A typical experiment. Once the chip has been fabricated, the course of an experiment is the following: we first degas the PDMS microchip in a vacuum container which will facilitate the subsequent filling of the chip; this is achieved by plugging a tubing containing a dilute colloidal suspension (volume fraction ϕ_0) and by pressurizing the tubing with a syringe until the liquid has totally penetrated the microsystem. As it takes a couple of minutes, the definition of the initial time of the experiment has an intrinsic error; however, this is small as compared to the typical timescale of the experiment of the order of hours.

The chip is then placed under a microscope whose settings are chosen according to the field of view we wish to observe: for the screening part, we use a stereo-microscope with a centimetre-large field of view, that allows scrutinizing the length of the many channels of the chip; we also use higher magnifications (*e.g.*, from 10× to 60× on a standard or a confocal microscope) in order to have a local view of the colloidal stacking. Series of images are captured with a charge-coupled device (CCD) camera, and

stored on a computer for automated post-treatment. The capture rate is tuned depending on the expected length of the experiment, and varies typically between 1 to 10 images per minute.

Immediately after placing the chip on the microscope, we start blowing dry air onto the membrane in order to ensure a constant environment. Not only does the stream remove vapor that permeates away, but importantly, it also keeps the humidity constant (and actually nearly zero) on the relevant side of the membrane. This is the driving force of the process and is essential to control as the ambient relative humidity may vary tremendously from day to day, typically from 30 to 80%.

2.2.4 Calibration. A key issue of the microevaporation technique is its ability to finely control the evaporation process. This is obvious from eqn (1) where the concentration rate of a solute directly depends on v_0 for instance, a quantity that relates directly to the actual evaporation rate. As the latter is minute [$\mathcal{O}$(nL min^{-1})], it is hard to measure it with great accuracy; weighting the mass loss of [$\mathcal{O}$(μg min^{-1})] is not accurate enough in our case.

We therefore developed a specific approach whose principle is the following: we fill the microsystem with deionized water and then dry up the reservoir. As the evaporation proceeds, an air/water meniscus invades the microchannels and propagates further inside, until it reaches the evaporation zone, and eventually the dead-end of the channel (see Fig. 3). Using image analysis, we automatically follow the positions of the menisci x_m against time for all microchannels in the calibration zone. We obtain a linear relationship $x_m \propto t$ which allows the unambiguous definition of a constant meniscus velocity at about 1% accuracy.

The calibration procedure is repeated up to ten times over time and all v_0 are averaged out at a given L_0, see the right part of Fig. 3. We actually dedicate one out of the 8 microevaporation groups on the chip specifically to calibration especially as even though deionized water was used, the repeated calibration procedure tends to pollute the tip of the capillary with impurities. We also designed a specific zone on the group for the calibration, located between the reservoir and the evaporation zone, where there is no evaporation and thus a constant $v_0(L_0)$, and is long enough to obtaining a good trajectory for the menisci (see Fig. 2). While a simple calibration yields an accuracy of about 1%, its repetition at different moments—and therefore at slightly different temperatures (controlled within 1 °C) and humidities (controlled relatively within 5%) but also and importantly at different ages of the chip—leads to a significant lowering of the accuracy, which finally gives v_0 of roughly ±10%. This will be the largest source of uncertainty in the work (note that such uncertainties could be reduced using systematic calibrations before and after each screening experiment, or using direct local velocity measurements on the flowing colloids).

The data reported in Fig. 3 are typical and collected systematically for every single chip. With v_0 in the range 5–15 μm s^{-1} for the L_0 used here, the corresponding time scale τ_e of the evaporation process is of the order of $L_0/v_0 \approx 400$ s. We however observe that the relationship between v_0 and L_0 is affine rather than linear: $v_0 = v_L + \alpha L_0$. We call v_L the leakage velocity which shows that even when $L_0 \to 0$, there is a non-vanishing, residual velocity that probably originates from permeation across the walls at the level of the tip of the microevaporator. As $v_L \approx 0.2$ μm s^{-1} remains moderate compared to v_0, we will neglect its effect in the rest of this work, although keeping in mind that the body of an ideal microevaporator should most likely be made out of glass to definitively suppress this effect and with only the membrane made of a permeable material.

3. Nucleation and growth of colloidal dense states

3.1 Close-up on nucleation and growth

We illustrate first the concentration kinetics of colloids with localized views at the level of the tip of a single microevaporator, see Fig. 4. The device is filled with a dilute dispersion of colloids

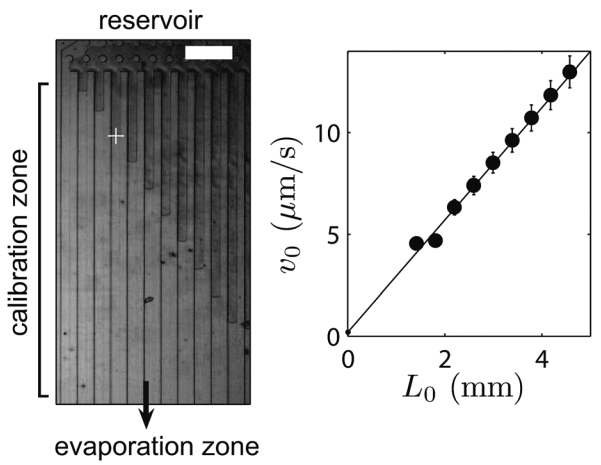

Fig. 3 Left: picture of the air/water menisci invading the microchannels as the evaporation proceeds at the level of the evaporators (outside the image); the bar represents 100 μm and the white + shows the image-processed localization of one meniscus. Right: velocity of the menisci measured by image analysis and averaged over about 10 runs, and plotted against the length L_0 of the evaporation channels.

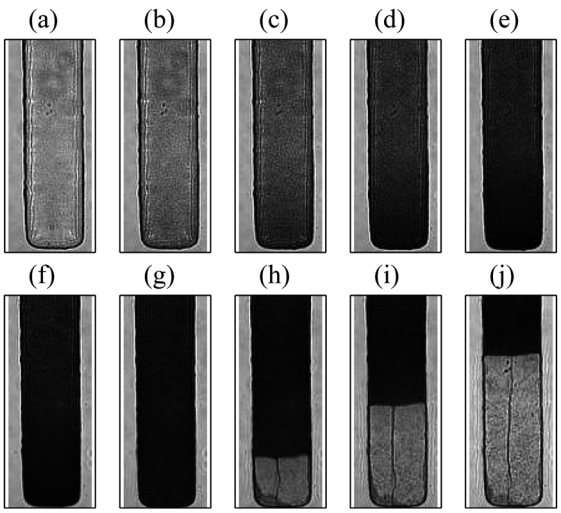

Fig. 4 Series of snapshots obtained at the level of the tip of a single microevaporator (width 50 μm) during the concentration kinetics of the colloidal suspension ($\phi_0 = 0.3\%$). The time elapsed between two consecutive images is $\delta t = 15$ min.†

($\phi_0 = 0.3\%$) and appears initially transparent (Fig. 4a); it becomes progressively more and more opaque (Fig. 4b–g) upon the accumulation of colloids at the level of the tip. At a given time, a front appears and progresses toward the reservoir (Fig. 4h–j); this front separates a relatively transmitting zone from the downstream opaque one†. This difference in transmission of the visible light thus suggests the growth of a colloidal organized texture leading to specific photonic properties.

Put another way, we observe for colloids what we also observed for electrolytes,[28] surfactant molecules,[29] and smaller charged nanoparticles,[31] that is the nucleation and growth of a specific texture. However, we will see next that both the nucleation and growth scenarios are significantly different and quite specific to these colloids.

3.2 Screening nucleation and growth

We use the screening chip to systematically study these nucleation and growth kinetics. In a typical experiment, we access several (nine) nucleation events followed by subsequent growth kinetics. We also repeated this experiment for several initial concentrations ϕ_0 and evaporation rates (translated into τ_e). To extract quantitative measurements, we systematically process our series of images in the following way: in a screening chip, we first identify the location of each channel and then get the intensity profile $I_k(x)$ along the k-th channel (between $x = 0$ and $x = L_0^{(k)}$), at every time step of the experiment.

We then analyze the profiles in order to extract the position of the front x_d against time for every L_0. The snapshot of Fig. 5 (left) indeed suggests that this position is readily accessible due to the high contrast between the dense and the dilute zones, thanks to the space derivatives of $I_k(x, t)$ which show extrema at $x = x_d$. The trajectory $x_d(t)$ is then plotted for different growth conditions, *i.e.*, different L_0 (Fig. 5, right). The results we collect follow a definite trend: after a given time τ_N, the growth initiates with a given velocity (of the order of 1 μm s^{-1}) which progressively slows down, as obvious from the bend of the front trajectory; later on ($t \gg \tau_N$), a linear growth behavior $x_d(t) \sim t$ settles in.

Such kinetics are directly affected by the operational parameters L_0 and τ_e. Fig. 5 (right) shows several trajectories for different L_0 while the insert of Fig. 5 shows the same data rescaled by the length of the respective evaporation channels x_d/L_0 and the time by the evaporation time t/τ_e. All the growth kinetics collapse onto a single curve, therefore evidencing the neat control imparted by the microevaporation tool onto the growth process. Note also that the τ_N we measure does not depend on L_0. We will give in the next section a simple model that explains most of these results.

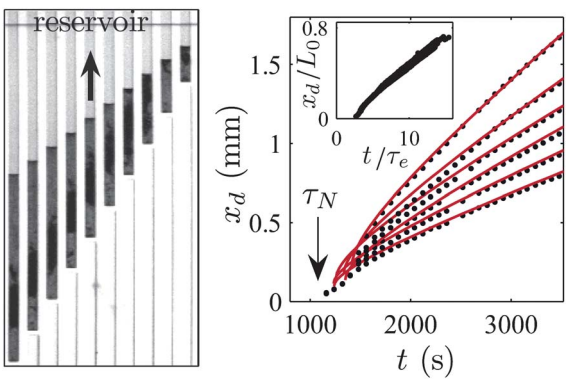

Fig. 5 Left: snapshot of the far-field view of the growth of dense states of colloids as observed in the screening chip; every single digit behaves as in Fig. 4. Right: front position x_d against time obtained by automated image analysis, for several lengths of microevaporators. The symbols correspond to the front positions and the solid lines to the simplified growth model given in the text [eqn (10)]. Insert: same data rescaled with the natural dimensions of every channel, *i.e.*, rescaled fronts x_d/L_0 against reduced time t/τ_e.

3.3 Rescaling of fronts

We go a step further by rescaling the data collected in very different conditions as obtained for different τ_e (because of a different fabrication procedure) and also for different ϕ_0. Note for instance in the insert of Fig. 6 top, that the evaporation time τ_e spans nearly one order of magnitude, while both ϕ_0 and L_0 vary by a factor of about 5 to 10. For a single screening experiment, we obtain a bundle of trajectories which display a growth kinetics close to the one we just described. Yet, as our experimental parameters vary tremendously, the different bundles are significantly shifted, see Fig. 6, top.

The natural rescaling comes from eqn (1) where the concentration rate scales like $L_0\phi_0$ and the time like τ_e. Using these new variables for rescaling the experimental data (Fig. 6, bottom), we observe that all the bundles reduce to a single master curve with a linear trajectory $x_d/L_0\phi_0 \sim t$. This representation somewhat hides the bend at the early stage of the growth ($t/\tau_e \lesssim 10$, insert of Fig. 5) but dilates the time and reveals what was not obvious in

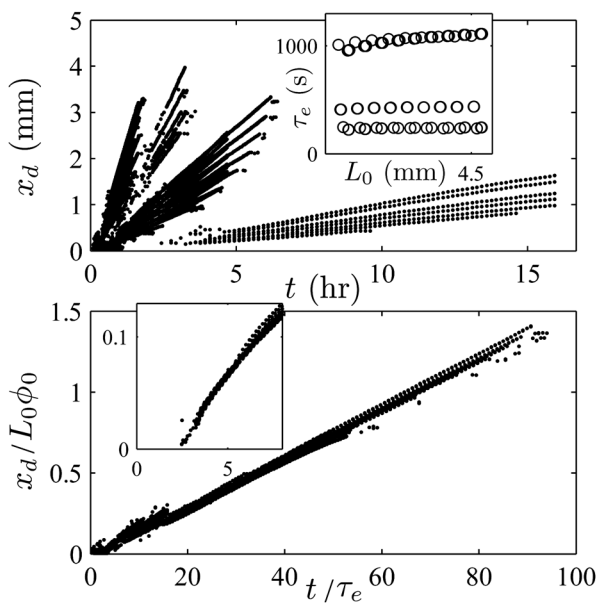

Fig. 6 Top: different series of growth kinetics collected in the screening chip for various ϕ_0 and with different evaporation rates (τ_e given in the insert, measured by calibration for several microsystems). Every bundle of curves is the outcome of one screening experiment. Bottom: rescaling of the front position $x_d/(L_0\phi_0)$ (ϕ_0 in %) against reduced time t/τ_e. Insert: same data but on short time scales.

Fig. 5, namely a constant growth velocity $v_d = \dot{x}_d$ at the late stage of the growth ($t/\tau_e > 10$).

While the whole behavior cannot be described without a (simple yet) complete model, this linear growth behavior is based on the mass conservation of colloids inside the evaporation zone: all the colloids that get accumulated induce the growth of the dense texture at a concentration ϕ_d. Assuming that the presence of colloids does not alter the evaporation rate, and that the concentration in front of the dense assembly is small compared to ϕ_d, a naive balance between the incoming flux and the growth rate leads to $\phi_0 v_0 \approx \phi_d v_d$ where ϕ_d is the volume fraction of the growing phase with a front velocity v_d. Therefore $v_d \approx (\phi_0/\phi_d)L_0/\tau_e$, and the slope of Fig. 6, bottom, directly gives $1/\phi_d$ (these results also suggest that the density of the growing texture does not depend on the location x). The estimate we obtain, $\phi_d \approx 66\%$, shows that the growing texture is actually a very dense state of colloids, but we cannot determine from such global measurements the exact nature of the texture (crystalline/glassy/polycrystalline).

4. Modeling nucleation and growth

4.1 Full description

Following Schindler and Ajdari,[35] we write the two basic equations of microevaporation that describe how a net flow in a simple binary mixture is induced by a concentration-dependent evaporation sink of one of the two species, which in turn translates into a concentration mechanism:

$$\partial_x v = -q(\phi), \tag{2}$$

$$\partial_t \phi = -\partial_x[\phi v(x) - D(\phi)\partial_x \phi]. \tag{3}$$

Here, $v(x)$ is the volume fraction weighted mixture velocity (averaged over the height and width of the channel), ∂_t and ∂_x are partial derivatives with respect to time and space. $q(\phi)$ is a sink term (1/s) and reflects the loss of water *via* pervaporation, and $D(\phi)$ is a mutual interdiffusion coefficient, also called a gradient or long-time collective diffusion coefficient.[36,37]

Eqn (2) and (3) can be solved numerically simultaneously to calculate the concentration process $\phi(x, t)$ of any binary aqueous solution or dispersion once both its thermodynamic and kinetic properties are known [$q(\phi)$ and $D(\phi)$]. The former controls the chemical potential of water against concentration which then affects the magnitude of the driving force (evaporation-induced velocity v). $D(\phi)$ results from an interplay between osmotic response and hydrodynamic interactions, as exemplified below in the context of colloidal dispersions,[36,37] and controls how solutes concentrate by the evaporation-induced flow.

4.2 Numerics on hard-sphere colloids

Although our colloids interact *via* electrostatics, the actual Debye length is small enough to be neglected against the size of the objects ($\lambda_D < 10$ nm at the working ionic strengths thus $R_p/\lambda_D \gg 1$), and we may assume that the colloidal system indeed behaves similarly to hard-sphere (HS) colloids with presumably an effective radius $R_{eff} \gtrsim R_p$ that accounts for an excluded volume due to short-range interactions.[36]

Interestingly, evaporation is not altered by the presence of colloids for HS colloids, that is $q(\phi) \approx$ const. Evaporation proceeds as for pure water, essentially because the modification of the chemical potential of water in a colloidal dispersion scales like $\Delta\mu_w \sim k_B T\phi Z(\phi) V_s/V_p \ll k_B T$, where $k_B T$ is the thermal energy, V_s is the volume of solvent molecules, V_p that of particles, and $Z(\phi)$ the osmotic compressibility of the dispersion. The very large contrast of volumes ($V_s/V_p \approx 10^{-10}$) ensures an almost constant chemical potential, and it holds until the ultimate compression of the densest phase that may occur. Therefore, eqn (2) becomes concentration independent and thus admits a simple solution: the velocity induced by evaporation is a simple linear function of the distance from the tip $v(x) \equiv -x/\tau_e$ (complementary measurements using particle tracking velocimetry on fluorescent tracers also confirm this result, data not shown).

Actually, the very large compression may also cause an irreversible aggregation of the colloidal dispersion as shown recently by Goehring *et al.*[22] in a similar context (see the discussion later in the text). In that case, evaporation still proceeds as flow is always possible across the porous structure. The chemical potential of water may now change because the viscous dissipation across the dense colloidal assembly may decrease the water pressure. This slowing down of the evaporation rate, due to a simple Kelvin effect, occurs when the water pressure drops below $\approx n_L k_B T \approx 1380$ Bar (n_L is the density of water molecules). Simple estimates of the pressure drop across a dense assembly of colloids of radii $R = 250$ nm (and with a typical length of several millimetres) using the Carmen–Koseny equation (that only involves volume fraction ϕ, and not the detailed structure of the texture), demonstrate that this subtle effect of a slowing down of the evaporation rate does not occur in our experiments. We recognize however that it may occur for smaller colloids, and it may explain some of the results observed by Dufresne *et al.*[38] in similar experiments but with smaller nanoparticles (radii < 30 nm).

Based on such a simple velocity profile, the concentration process can then be calculated numerically if $D(\phi)$ is postulated. For a colloidal dispersion, the long-time collective diffusion coefficient $D(\phi)$ follows:

$$D(\phi) = D_0 K(\phi) \frac{\mathrm{d}\phi Z(\phi)}{\mathrm{d}\phi}, \tag{4}$$

where D_0 is the Stoke-Einstein diffusion coefficient of a single sphere (for $\phi \to 0$), and $K(\phi)$ is the sedimentation factor (ratio of the sedimentation velocity at ϕ over that at $\phi \to 0$).[36,37,39] This last relation, often called the generalised Stokes–Einstein equation, indicates that the relaxation of density gradients comes from a competition between colloidal interactions (the osmotic compressibility term) and hydrodynamic flows in the suspension (sedimentation factor).[36,37,39]

Assuming HS interactions, we use analytical formula for $K(\phi)$ and $Z(\phi)$ that have been extrapolated from numerous experimental data or theoretical calculations on a broad range of volume fractions. For the osmotic term, we use:

$$Z(\phi) = \frac{1 + a_1\phi + a_2\phi^2 + a_3\phi^3 + a_4\phi^4}{1 - \phi/\phi_c},$$

with $a_1 = 4 - 1/\phi_c$, $a_2 = 10 - 4/\phi_c$, $a_3 = 18 - 10/\phi_c$, and $a_4 = 1.85/\phi_c^5 - 18/\phi_c$ with $\phi_c = 0.64$. This formula derived by Peppin *et al.*,[21] matches asymptotically the results of Carnahan–Starling valid for $\phi < 0.55$ and those of Woodcook $Z(\phi) \approx 1.85/(\phi_c - \phi)$ valid for $\phi \to \phi_c$.[36,40–42] Note that we chose not to include crystallization at this stage (as done recently by Style and Peppin[43]) and therefore, this description concerns solely a colloidal suspension that becomes glassy at ϕ_c; we shall discuss this issue later in the text. For the hydrodynamic interactions, we use $K(\phi) = (1 - \phi)^{6.55}$,[44] but many other formula exist and are each slightly different (*e.g.*, permeability of HS suspensions[45]), yet deliver the same qualitative behavior since in all cases $K(\phi)$ stays finite at ϕ_c.

The resulting diffusion coefficient is plotted in Fig. 7 (insert) and shows that between $\phi = 0$ and $\phi \lesssim \phi_c$, $D(\phi)$ is hardly affected by the concentration: the two effects of magnified driving force and increased dissipation cancel out to give a diffusion coefficient that varies non-monotically by at most a factor of 2.[36] Instead, at $\phi \approx \phi_c$, $D(\phi)$ shoots up and diverges because of the divergence of the osmotic compressibility, at a finite $K(\phi)$.

Numerically, we solve eqn (3) with the values for $D(\phi)$ described before using a non-dimensionalized equation where $X = x/L_0$, $T = t/\tau_e$, $V = v/(L_0/\tau_e)$:

$$\partial_T \phi = -\partial_X \left[-\phi X - \frac{\hat{D}(\phi)}{Pe} \partial_X \phi \right]. \quad (5)$$

The bare Péclet number emerges as $Pe = L_0^2/D_0\tau_e \equiv v_0 L_0/D_0$, and $\hat{D}(\phi) = D(\phi)/D_0$ [eqn (4) and insert of Fig. 7] actually accounts for the non-linearity of the collective diffusion coefficient $D(\phi)$.

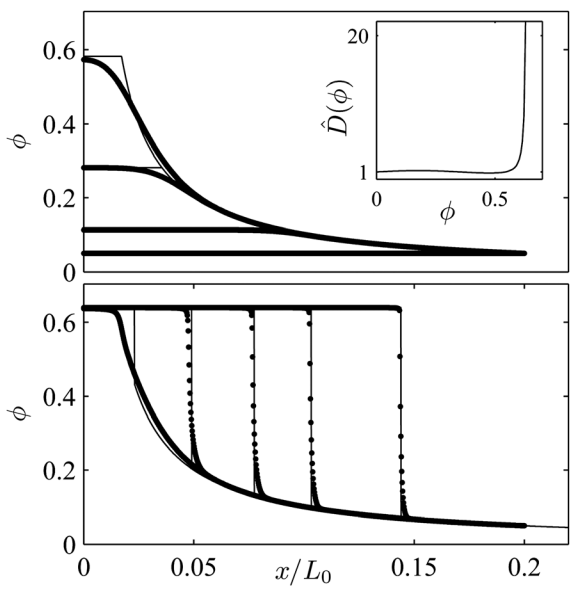

Fig. 7 Volume fraction profiles (real units) against x/L_0 calculated numerically (symbols) with the diffusion coefficient $\hat{D}(\phi) = D(\phi)/D_0$ shown in the insert [D_0 is the Stoke-Einstein diffusion coefficient of a single sphere and $D(\phi)$ is calculated from eqn (4) with $\phi_c = 0.64$] and analytically (lines) following the naive model given the text (Péclet number $Pe = 10^4$, $\phi_0 = 0.01$). (Top) initial stage of the concentration process (times $T = 1.61$, 2.43, 3.34, and 4.06); (bottom) after induction and growth of a dense state ($T = 4.25$, 5.15, 6.52, 7.88, and 10.15).

For the colloidal systems of interest here, Péclet numbers are gigantic, $Pe \approx 10^3$–10^6.§ In these conditions, numerical solutions of the model show (Fig. 7) a concentration process whereby colloids are accumulated at the tip of the evaporator up to a concentration that leads to the occurrence of a state that grows at $\phi \approx \phi_c$. This behavior originates from the divergence of $D(\phi)$ for $\phi \to \phi_c$: the system cannot sustain concentration gradients as the mutual diffusivity becomes very large. Facing the impossibility of becoming more concentrated, the colloidal suspension expands instead and invades the evaporator at $\phi \approx \phi_c$.

Importantly here, and as already pointed by Schindler and Ajdari,[35] the origin of this growth comes from the divergence of the compressibility whereas $K(\phi)$ remains finite, up to ϕ_c (and in fact whatever $\phi_c < 1$) which amounts to say that the dense state that grew is porous. Although somewhat obvious for colloidal spheres, it matters for the growth process: flow is always possible across the structure, driven by the evaporation of water which hardly feels the presence of colloids, but still exerts a viscous friction on the structure. Regardless of the exact structure—namely a glass, a perfect or defective poly-crystal—the scenario does not change; these dense states remain porous [finite $K(\phi)$] but become hardly compressible at a certain concentration, which triggers the growth.

4.3 A toy model for hard-sphere colloids

In order to better catch in a simpler way, the mechanisms at work during the concentration process, we propose a simplified version of the case described above. The core idea is that the suspension is *essentially convected* toward the tip of the micro-evaporator, until it reaches a maximal concentration ϕ_d, corresponding to a dense and thus incompressible state. Then, this state grows as constantly fed by a predictable flux of convected particles. This hypothesis holds since Pe $\gg$ 1 (negligible gradient diffusion coefficient), and a *simple conservation law based on the convective current only* $j(x) = \phi(x)v(x) = \text{const} = \phi_0 v_0$ is sufficient. We now calculate the concentration profiles until $\phi = \phi_d$ using previously published solutions of the microevaporation equation,[46] and then we calculate the growth dynamics of the dense state at ϕ_d.

4.3.1 Nucleation. For $Pe \gg 1$, the solute conservation equation [eqn (5)] simplifies to:

$$\partial_T \phi = \phi + X \partial_X \phi, \quad (6)$$

which admits analytical solutions:[46] in the steady state ($\partial_T \phi = 0$), we recover the base-line hyperbolic branch $\phi(X)/\phi_0 = 1/X$, while the transient regime leading to this steady state admits a piece-wise solution:

$$\phi(X, T)/\phi_0 = \exp T \quad \text{for } T < -\ln X, \quad (7)$$

$$\phi(X)/\phi_0 = 1/X \quad \text{either.}$$

The Fig. 7 (top) shows the concentration profiles calculated at several times using this simplified model with a solid line. One can

§ $\tau_e \approx$ 200–1000 s, $L_0 \approx$ 1–10 mm, and $D_0 \approx 10^{-12}$ m^2 s^{-1}.

see the hyperbolic branch connected to a concentration plateau, the latter shrinks as it raises exponentially with time [eqn (7)].

This increase of concentration stops whenever $\phi = \phi_d$ somewhere in the system; it occurs of course at the tip of the channel at a time we call (somewhat abusively) the dimensionless nucleation time:

$$T_N = \ln(\phi_d/\phi_0), \tag{8}$$

at which the arrested zone at ϕ_d occupies a finite spatial extent $X_N = \phi_0/\phi_d$.

4.3.2 Growth. Admitting that $D(\phi \to \phi_d) \to \infty$, the dense phase cannot get compressed and must grow, and we describe the pace at which it occurs using a direct conservation law: all the colloids that enter the microsystem with a flux $\phi_0 V_0$ are convected downstream and contribute to grow the dense phase at a velocity $V_d = dX_d/dT$, where X_d now refers to the front position (capital letters stand for dimensionless units). The dense phase grows in a concentration field which is not uniform and depends specifically on the actual position $X_d(T)$ of the front, the flux balance thus reads:

$$[\phi_d - \phi(X_d)]V_d = \phi_0 V_0, \tag{9}$$

which we integrate between the nucleation at T_N and the actual time T to obtain the trajectory of the front:

$$\frac{\phi_d}{\phi_0}X_d(T) - 1 - \ln\left[\frac{\phi_d}{\phi_0}X_d(T)\right] = T - T_N. \tag{10}$$

This trajectory describes the position of the front between a phase at ϕ_d for $X < X_d$ and the hyperbolic concentration ramp $\phi = \phi_0/X$ for $X > X_d$.

The direct comparison of the concentration profiles against space and time during the concentration process between the numerics and the toy model with $\phi_d = \phi_c$ (Fig. 7) shows an overall excellent agreement either before or after nucleation. Concentration profiles are roughly correct at small X where diffusion matters (and explain the discrepancy), but display an excellent agreement at later times with profiles which are nearly perfectly described by the simplified model. It shows that diffusion is indeed negligible and that the growth kinetics are adequately caught solely by the conservation law.

4.4 Comparison with experiments

We now propose to test our toy model assuming that the numerics with the neat description of the transport quantities [Fig. 7, exact numerical solution of eqn (3), and (4)] represent a trustworthy basis.[35] We fit all our experimental trajectories of dense states collected for many ϕ_0, τ_e, and L_0 (*e.g.*, Fig. 5 and 6) using eqn (10) where both T_N and ϕ_d are adjustable parameters. The results are reasonably convincing, see for instance Fig. 5, where the solid lines are superimposed to the experimental data and describe correctly the bend at the early stage of the growth and rather well the growth kinetics later on.

Because there is no effect on the operational parameter L_0 or on the nucleation time T_N on the dense phase concentration ϕ_d (see the rescaling in Fig. 5), each screening experiment performed on 9 different L_0 leads to a unique set of parameters T_N and ϕ_d. Fig. 8 shows that for several τ_e and ϕ_0, the nucleation time is correctly described by the one predicted by our simplified model [see eqn (8)], namely $\tau_N = \tau_e \ln(\phi_d/\phi_0)$ where we adjusted $\phi_d = 0.65$ with a modest yet reasonable accuracy, about $\pm 15\%$. The insert of Fig. 8 indicates the second outcome of the fitting procedure, *i.e.*, the concentration of the growing dense phase, ϕ_d. Again, the fitted ϕ_d are in the range 55–70%, and this large source of uncertainty essentially originates from that of the calibration procedure—measurements of v_0 which in turn affect τ_e—whereas the tracking of the front delivers a very precise result.

We can also now catch some features of the growth mechanisms. Focusing first at the late stage of the growth, that is $X_d(T) \gg X_N = \phi_0/\phi_d$ for $T \gg T_N$, and with also $\phi_0/\phi_d \ll 1$ so that eqn (10) simplifies to:

$$X_d(T) \approx \frac{\phi_0}{\phi_d}T, \text{ that is } x_d(t) \approx L_0\frac{\phi_0}{\phi_d}\frac{t}{\tau_e} \tag{11}$$

with real units: the late growth is linear. This explains and justifies the good rescaling of Fig. 6 with the growth chiefly controlled by the geometry (L_0) and the dispersion in the reservoir (ϕ_0) which together deliver a current $\propto L_0\phi_0$, and the kinetics (τ_e) which provides the pace to the process. It eventually delivers a way to measure ϕ_d, as done earlier on the basis of scaling arguments to obtain $\phi_d \approx 0.66$. Another way to understand it relies on eqn (9) for which $\phi(X_d) \approx \phi_0 \ll \phi_d$, and thus the dense phase grows in a negligible and constant concentration field (close to ϕ_0) with a constant velocity.

This contrasts strongly with what happens at the early stage of the growth: as the phase just nucleated ($X_d \gtrsim X_N$), the nucleation points not so far from the tip of the evaporator where the hyperbolic concentration profile $\phi = \phi_0/X$ delivers a high concentration; the dense state is thus fed by a rich dispersion and grows quickly. We thus expect the growth velocity to be high close to the nucleation point and then to slow down progressively

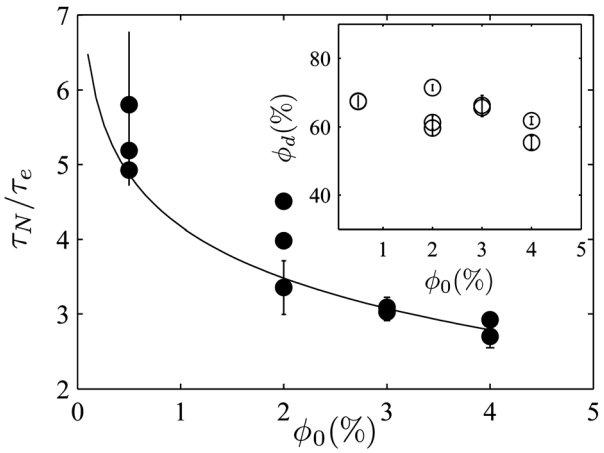

Fig. 8 Reduced nucleation time $T_N = \tau_N/\tau_e$ against the initial volume fraction ϕ_0 where each solid circle represents about 10 measurements; the solid line represents the simplified model $T_N = \ln(\phi_d/\phi_0)$ where $\phi_d = 0.65$ in this case. The insert represents the second outcome of the fitting procedure, ϕ_d, against the initial volume fraction; each shown value represents an average over about 10 measurements.

to reach the regime described above, solely governed by control parameters. We believe it explains the bends we observe for instance in Fig. 5.

5. Toward local structures and the role of ionic strength

The main achievement of the previous model is to provide a simple and predictive view on a complex process—the growth of colloidal structures in confined geometries—and to deliver near-quantitative information on the growing phase. However, as a global measurement, the tracking of the front only misses some fine details, for instance on structural transitions that may occur during growth. After the previous global observations, we thus turn to a local characterization of the structure using several complementary techniques to improve the understanding of the phenomena.

5.1 Local measurements: ordered *vs.* disordered textures

Several textures during the growth of the colloidal dense phase were first noticed by optical microscopy in transmission mode (see Fig. 9A). Indeed, we often observe an alternative sequence: the dense state grows initially transmissive, then opaque, and then transmissive again. We also observe that both the color and the texture correlate to the transmission of light: the sample goes from pink-reddish in the transmitting case with well-defined boundaries that separate slightly different colors, to yellow-brown in the opaque case (Fig. 9B) with an homogeneous microstructure.

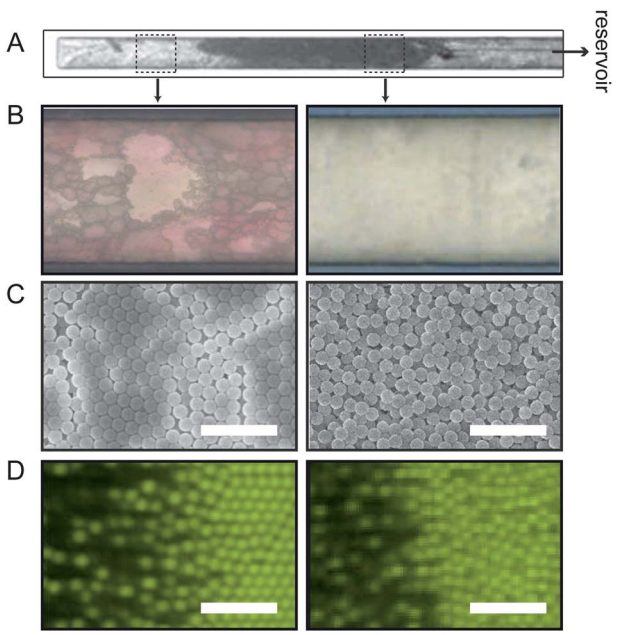

Fig. 9 (A) Far-field view of the typical sequence observed during the growth of the dense colloidal assembly: ordered → disordered → ordered textures (the dotted rectangles indicate schematically the positions of the ordered and disordered textures in (B–C)). (B–D) Comparison between the ordered and disordered structures using optical microscopy in transmission geometry (B), scanning electron microscopy of extracted samples (C), and confocal optical microscopy (D) at the level of the growing front.† A and B: the width of the channels is 50 μm. C and D, the white bars correspond to 3 μm.

If we use a white light to shine the microsystem containing the dense states, we observe in the first case a bright and vivid opalescence, giving spectacular colors at given angles; they can also be seen in the picture of Fig. 2. In the second case, we observe no iridescence at all. We thus call the first texture an ordered structure, as opposed to the disordered structure of the second texture, relying on the Bragg reflections as a signature of the colloidal ordering. The difference between this disordered state and the crystalline state can also be evidenced during the growth process using confocal microscopy, see Fig. 9D where the snapshots are localized at the level of the growing front, between the dilute and the dense phases whose structures are clearly different (see also the corresponding movies in the ESI†).

To obtain further evidence of these structures, we used scanning electron microscopy (SEM) to visually probe the colloidal ordering. This technique has two major drawbacks: it requires drying of the microdevice which may induce fractures in the dense colloidal state. It also requires peeling off the membrane of the microdevice to access the structure and the addition of a thin layer of metal to enhance the contrast. However, it gives a direct and visual access to the structures at the surface of the dense state and in its bulk thanks to the fractures. We indeed confirmed that the structural assumptions given above and based on optical properties are related to a local ordering or disordering of the colloids (Fig. 9C).

5.2 Failure of the analogy with sedimentation

These detailed observations show that several structures are possible during the growth of the dense state. Such a result is reminiscent of the seminal works of Davis and coworkers[19,44] concerning the possible transition between crystals and glasses during sedimentation of HS colloids. Indeed, either a glassy or a crystalline phase can grow during sedimentation, depending on the actual concentration rate of colloids close to the sediment (see the famous cover picture of Ref. 36). The competition between the two states relies on an interplay between the concentration rate and the growth rate of a nucleus, redefined by Davis *et al.*[19] in terms of a Péclet number calculated locally with the local velocity, the size of the particle, and the self-diffusion coefficient D_s: $Pe_L = vR_p/D_s$. A low local Péclet number yields organized structures, whereas a high Péclet number leads to a disordered, glassy-like texture. Similar observations in experiments of drying of colloidal suspensions[47,48] have also been explained in a same way, *i.e.*, as a competition between the drying kinetics and the crystallization kinetics.

Such an explanation fails in the context of our experiments. First, the local velocity, and so the local Péclet number $Pe_L = v(x)R_p/D_s$, increases continuously along the microevaporation zone (Fig. 2 top, blue arrows). The above argument cannot thus explain the alternative sequence observed in our experiments, crystal/disordered/crystal [see Fig. 9A]. Another argument is that even at much larger distances, and thus at even relatively large local Péclet number ($Pe_L \approx 3$ for $v_0 \approx 10\ \mu m\ s^{-1}$), the crystal can grow neatly without exhibiting a structural transition toward a glass. This may point out the role of hydrodynamics in

structuring the colloidal assembly. Indeed, unlike for sedimentation, there is a permanent flow of water across the porous dense colloidal assembly (evaporation persists downstream) which may register the colloids in crystalline sites, and thus help the formation of colloidal crystals.[24,49]

As demonstrated below, the true origin of the observed structural sequences comes from the presence of ionic species in our charge-stabilized dispersion.

5.3 The role of the ionic strength

5.3.1 Breakdown of the colloidal stability. We first noticed that depending on the added salt, we can roughly control the textures that grow, see Fig. 10A. Indeed, our colloidal suspension is charge-stabilized and the ionic strength is an important parameter for their phase diagram. We thus grew dense states with different known amounts of NaCl added to the initial dispersion to reach a salt concentration c_s (which also accounts for sodium azide present in the initial stock dispersion, see Sec. 2). Above a given salt concentration range (roughly 2 mM), the dense state grows totally opaque (Fig. 10A, bottom) along the microevaporator. For smaller ionic strength (<2 mM), we observed the alternative sequence detailed above, but the exact transition lines between the different states remained somewhat rough. Note that it is possible to pass from one scenario to the other by tuning the amount of added salt, however it turns out to be very difficult to control precisely.

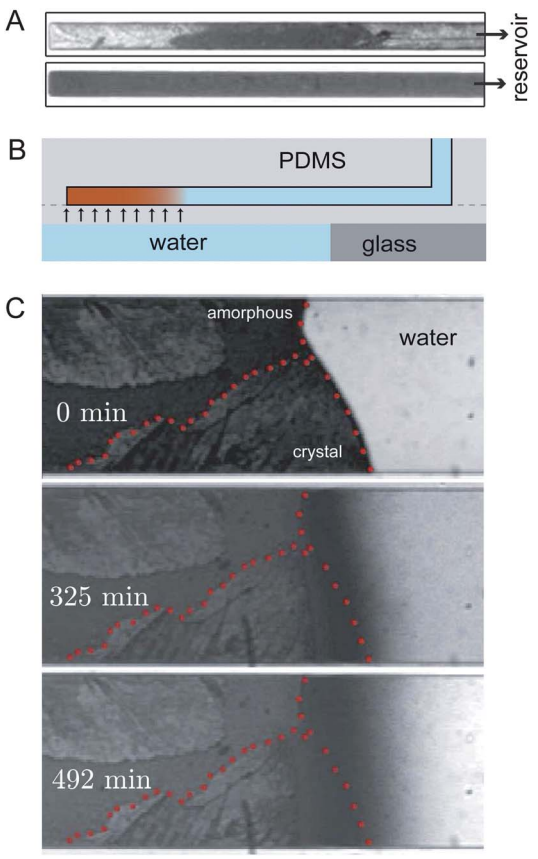

Fig. 10 (A) Far-field views of the sequence observed at low ionic strength (top), and of the disordered texture only observed at high added amount of NaCl (bottom). (B) Sketch of a re-dissolution experiment: the reservoir is first filled with water only (the incoming flux is turned to 0), then evaporation is stopped by placing water below the membrane. The difference in chemical potential induces an inverse flow that dissolves the microstructures. (C) Observations of the dissolution process close to the crystal-to-disordered transition, at different times $t = 0$ (steady-state), 325 and 492 min. The dotted lines indicate the initial positions of the disordered and ordered textures. Only the dissolution of the crystal occurs†.

5.3.2 Dissolution of the colloidal textures. While our previous growth model does not catch the origin of these structural transitions, we observed that they depend on the amount of added salt and we postulate that these transitions represent an example of the breakdown of colloidal stability due to the concentration of ions. To further assess it, we performed the following experiment (Fig. 10B). We first grew a dense colloidal assembly up to the first crystal-to-disordered texture transition. We then placed water in the reservoir to stop the incoming flux of solute; the system thus reaches a steady state (water still flows as evaporation is not stopped). Fig. 10C (top) shows a localized snapshot at the tip of the formed colloidal assembly: disordered textures (opaque regions) and crystals (transmissive ones) coexist and form rough patterns.

Finally, we placed water below the membrane in order to stop permeation, and thus the flow, and dissolve (or not) the dense colloidal assembly. Indeed, we expect that the chemical potential of water $\mu_w(\phi)$ is lower in the microchannel, thus inducing a reverse flow that can dissolve the formed textures (see arrows in Fig. 10B). Actually, only the crystalline parts dissolve, and the disordered texture remains intact during the experimental duration ($t \approx 500$ min, Fig. 10C). This result indicates that the disordered texture lost its colloidal nature, and again corroborates the breakdown of colloidal stability. Importantly, this points out that the disordered textures are not colloidal glasses, rather colloids that were packed randomly by the permeation-induced flow in an environment where they do not have their colloidal stability (*i.e.*, at high ionic strength). The crystalline regions however, re-dissolve under this flow: such a dense organized assembly was only maintained by the evaporation-induced flow. All these results again underline the importance of flow and local electrostatic repulsions in the formation of colloidal crystals in such a technique.

5.3.3 Qualitative scenario. These new insights also help us to give qualitative arguments to explain the alternative transitions, crystal → disordered → crystal, that occur in the microevaporator. These arguments rely on the competition between the concentration process of the colloids and that of the ionic species. Indeed, our suspensions both contain colloids (at a concentration $\phi_0 \approx 1\%$) and soluble ionic species (sodium azide, $c_s \approx 1$ mM), and microevaporation concentrates all of them. For dilute solutions or dispersions (see Sec. 2.2.1), the evaporation-induced flow concentrates solutes in an accumulation box of size $p \sim \sqrt{D\tau_e}$ at a rate given by eqn (1) (D is the diffusion coefficient of the solute in the dilute regime). In our experiments, colloids and ions thus concentrate simultaneously in different accumulation boxes, and at different rates. The accumulation rate for the colloids ($D_0 \approx 10^{-12}$ m^2 s^{-1}) is very

large, and the accumulation box size is very small ($p \approx 30$ μm for $\tau_e \approx 1000$ s, *i.e.*, convection dominates) compared to the ions ($D \approx 10^{-9}$ m^2 s^{-1}) accumulated slowly in a $p_s \approx 1$ mm box. Such a difference may lead to the following scenario. First, colloids are convected and concentrate rapidly at the tip of the microevaporator, in a low salt environment. Electrostatic repulsions are thus present, and rather well-defined colloidal crystals are formed. During the growth of the colloidal crystal, the salt concentration increases and may reach a critical value in the accumulation box $x < p_s$, for which colloidal stability is not ensured anymore. The lack of electrostatic repulsions does not guide the colloids to the right crystalline sites and an amorphous and porous state is formed during the accumulation of the colloids, since they are not stabilized anymore. Importantly, as soon as the colloidal packing grows beyond the accumulation box of the salt ($x > p_s \approx 1$ mm), the ionic strength decreases again, as ions are only convected here, and electrostatic repulsions are recovered. These recovered interactions, combined with the flow, probably help guide the formation of the colloidal crystallinity. In such a scenario, the position of the re-entrant transition (amorphous → crystal) should only depend on the size of the accumulation box of the ions, and not on geometrical parameters such as L_0. This is indeed observed in our experiments of tracking of the front (see Fig. 5).

5.3.4 Discussions. More detailed investigations (*e.g.*, systematic re-dissolution experiments…) should *a priori* be performed in the near future to firmly confirm the scenario proposed above. We believe however that all of our experiments point out the crucial role played by the ionic species on the ordering process. Note also that recent experiments performed by Goehring *et al.*[22] in the similar context of uni-directional solidification, demonstrated that the irreversible aggregation of colloids (and thus also a breakdown of colloidal stability) also occurs due to the strong compressive forces induced by the solvent flow. This general argument should also apply to our experiments because water still flows through the dense colloidal packing. However, we do not observe any sudden changes of colors in our colloidal crystals, that can be attributed to a collapse of the colloidal network as observed by Goehring *et al.*[22] We believe that such discrepancies probably come from the range of parameters explored in our work, as the permeation-induced flow may not be large enough to induce such effects. We thus plan to investigate such regimes by playing with the geometry: a longer microevaporator L_0, a smaller height h, and longer colloidal crystals (>1 cm) should *a priori* correspond to the regimes explored in Ref. 22. A very large *local* Péclet number Pe_L should also be reached for such a regime, and we hope to investigate its role on the ordering process, as recent similar experiments of drying observed amorphous structures due to large Pe_L only.[47,48]

6. Conclusions

In the present work, we managed to concentrate a dilute charge-stabilized dispersion in a controlled way, up to the growth of colloidal crystals, several mm long, in confined microchannels (typical transverse dimensions 10×50 μm^2). The benefits of microfluidics yield a precise control on the growth pace of the colloidal crystals thanks to tunable parameters (evaporation time τ_e, length L_0, initial concentration ϕ_0). Such a good control of the transport process of the colloids also permits the precise modelling of the growth rate of these dense colloidal assemblies using simple conservation laws. This modeling can take a very simple form because convection mostly dominates the concentration process, but also importantly because the colloidal dispersion behaves in a similar manner to hard-spheres, *i.e.*, it displays an almost constant collective diffusion coefficient $D(\phi)$ until it diverges. It becomes invalid for highly-charged colloidal dispersions or at very low ionic strength as electrostatic repulsions induce a large enhancement of $D(\phi)$ which in turn leads to a more complex concentration process.[31,50,51]

We also observe that depending on the initial ionic strength, amorphous structures can be formed during the concentration of the colloids. This feature is likely to come from the breakdown of the colloidal stability due to the concentration of ionic species initially present in the dilute dispersion (<1 mM). Moreover, the competition between the concentration of ions and colloids explain, at least qualitatively, the re-entrant sequence, crystal/amorphous structure/crystal, that is observed during the growth of the dense state. Such a result is probably relevant for other colloidal-assembly techniques, since both colloids and ions are simultaneously concentrated as soon as drying is used to reach high colloidal concentrations. A complete theoretical description of the concentration process of colloids up to dense states, also taking into account the concentration of ions (and thus possibly diffusiophoretic phenomena[52] and Donnan-like potentials…) is still missing. We believe that such a theoretical investigation may be a real challenge, as is the case for the related topic of sedimentation of charged colloids.[53]

The colloidal crystals formed using the present technique display many structural defects that may prevent their use for several key applications (*e.g.*, photonics). Such defects come from an intrinsic polydispersity of the dispersion, but are also largely due to the technique itself. Indeed, well-organized colloidal crystals are formed more easily on the large-scale using evaporation-induced self-assembly techniques, thus suggesting the important role played by the capillary forces and flow during self-assembly.[23] However, our technique may be relevant since a good control can be cast on the process using the geometrical features of the microfluidic chip. We plan therefore in the near future to investigate the role of the confinement and evaporation rate on the density of defects that are formed during colloidal growth. Moreover, the possibility to engineer complex geometries of microevaporators using the microfabrication toolbox (such as topographical patterns for instance) may lead to original investigations of the link between the colloidal growth and the geometry of the confined cell. Importantly, complex sequences of concentration can also be done relatively easily with the microevaporation technique. We can indeed change, in time, the chemical composition of the reservoir containing the dispersion to be concentrated (Fig. 11). This unique feature (combined with the possibility of manufacturing complex geometries) open the way to designing complex architectures displaying well-defined sequences of dense states of colloids, polymers, or other solutes, organized at the microfluidic scale.

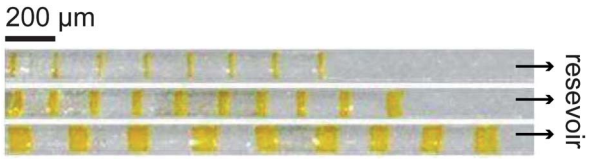

Fig. 11 Three examples of super-structures induced by the micro-evaporation of colloids (diameter 100 nm, $\phi_0 = 0.1\%$) where the composition in the reservoir is regularly changed between bare particles and fluorescent particles; the accumulation time of the bare particles is constant while the accumulation time of the fluorescent particles is doubled at each line from top to bottom of the image.

Acknowledgements

We thank Région Aquitaine, Université Bordeaux-1, Rhodia, and CNRS for funding and support.

References

1 O. D. Velev and S. Gupta, *Adv. Mater.*, 2009, **21**, 1.
2 P. Podsiadlo, G. Krylova, A. Demortière and E. Shevchenko, *J. Nanopart. Res.*, 2011, **13**, 15.
3 P. Jiang, J. F. Bertone, K. S. Hwang and V. L. Colvin, *Chem. Mater.*, 1999, **11**, 2132.
4 E. Kim, Y. Xia and G. M. Whitesides, *Adv. Mater.*, 1996, **8**, 245.
5 Y. A. Vlasov, X.-Z. Bo, J. C. Sturm and D. J. Norris, *Nature*, 2001, **414**, 289.
6 S. Wong, V. Kitaev and G. O. Ozin, *J. Am. Chem. Soc.*, 2003, **125**, 15589.
7 R. Mayoral, J. Requena, J. S. Moya, C. Lopez, A. Cintas, L. Vasquez, M. Holgado and A. Blanco, *Adv. Mater.*, 1997, **9**, 257.
8 A. van Blaaderen, R. Ruel and P. Wiltzius, *Nature*, 1997, **385**, 321.
9 O. D. Velev, T. A. Jede, R. F. Lobo and A. M. Lenhoff, *Nature*, 1997, **389**, 447.
10 B. Gates, D. Qin and K. Q. Xia, *Adv. Mater.*, 1999, **11**, 466.
11 Y. Masuda, T. Itoh and K. Koumoto, *Langmuir*, 2005, **21**, 4478.
12 M. Ishii, H. Nakamura, H. Nakano, A. Tsukigase and M. Harada, *Langmuir*, 2005, **21**, 5367.
13 C. Sun, X. W. Zhao, Y. J. Zhao, R. Zhu and Z. Z. Gu, *Small*, 2008, **4**, 592.
14 M. Abkarian, J. Nunes and H. A. Stone, *J. Am. Chem. Soc.*, 2004, **126**, 5978.
15 S. Hu, Y. Men, S. V. Roth, R. Gehrke and J. Rieger, *Langmuir*, 2008, **24**, 1617.
16 A. D. Dinsmore, J. C. Crocker and A. G. Yodh, *Curr. Opin. Colloid Interface Sci.*, 1998, **3**, 5.
17 N. V. Dziomkina and G. J. Vancso, *Soft Matter*, 2005, **1**, 265.
18 G. Jing., H. Bodiguel, F. Doumenc, E. Sultan and B. Guerrier, *Langmuir*, 2010, **26**, 2288.
19 K. E. Davis, W. B. Russel and W. J. Glantschnig, *J. Chem. Soc., Faraday Trans.*, 1991, **87**, 411.
20 R. D. Deegan, M. Balkanski, T. F. Dupont, G. Huber, S. R. Nagel and T. Witten, *Nature*, 1997, **389**, 827.
21 S. S. Peppin, J. A. Elliott and M. G. Worster, *J. Fluid Mech.*, 2006, **554**, 147.
22 L. Goehring, W. J. Clegg and A. F. Routh, *Langmuir*, 2010, **26**, 9269.
23 D. J. Norris, E. G. Arlinghaus, L. Meng, R. Heiny and L. E. Scriven, *Adv. Mater.*, 2004, **16**, 1393.
24 D. D. Brewer, J. Allen, M. R. Miller, J. M. de Santos, S. Kumar, D. J. Norris, M. Tsapatsis and L. E. Scriven, *Langmuir*, 2008, **24**, 13683.
25 A. S. Dimitrov and K. Nagayama, *Langmuir*, 1996, **12**, 1303.
26 G. M. Walker and D. J. Beebe, *Lab Chip*, 2002, **2**, 57.
27 J. C. Eijkel, J. G. Bomer and A. van der Berg, *Appl. Phys. Lett.*, 2005, **87**, 114103.
28 J. Leng, B. Lonetti, P. Tabeling, M. Joanicot and A. Ajdari, *Phys. Rev. Lett.*, 2006, **96**, 084503.
29 J. Leng, M. Joanicot and A. Ajdari, *Langmuir*, 2007, **23**, 2315.
30 P. Moreau, J. Dehmoune, J. B. Salmon and J. Leng, *Appl. Phys. Lett.*, 2009, **95**, 033108.
31 A. Merlin, J. Angly, L. Daubersies, C. Madeira, S. Schöder, J. Leng and J. B. Salmon, *Eur. Phys. J. E*, 2011, **34**, 58.
32 X. Noblin, L. Mahadevan, I. A. Coomaraswamy, D. A. Weitz, N. M. Holbrook and M. A. Zwieniecki, *Proc. Natl. Acad. Sci. U. S. A.*, 2008, **105**, 9140.
33 J. C. Mcdonald and G. M. Whitesides, *Acc. Chem. Res.*, 2002, **35**, 491.
34 M. A. Unger, H. P. Chou, T. Thorsen, A. Scherer and S. R. Quake, *Science*, 2000, **288**, 113.
35 M. Schindler and A. Ajdari, *Eur. Phys. J. E*, 2009, **28**, 27.
36 W. B. Russel, D. A. Saville and W. R. Schowalter, *Colloidal dispersions*, Cambridge University Press, 1989.
37 G. Nägele, *The Physics of Colloidal Soft Matter*, Polish Academy of Sciences publication, Warsaw, 2004.
38 E. R. Dufresne, E. I. Corwin, N. A. Greenblatt, J. Ashmore, D. Y. Wang, A. D. Dinsmore, J. X. Cheng, X. Xie, J. W. Hutchinson and D. A. Weitz, *Phys. Rev. Lett.*, 2003, **91**, 224501.
39 W. R. Bowen, Y. Liang and P. M. Williams, *Chem. Eng. Sci.*, 2000, **55**, 2359.
40 N. F. Carnahan and K. E. Starling, *J. Chem. Phys.*, 1969, **51**, 635.
41 S. E. Phan, W. B. Russel, Z. Cheng, J. Zhu, P. M. Chaikin, J. H. Dunsmuir and R. H. Ottewill, *Phys. Rev. E: Stat. Phys., Plasmas, Fluids, Relat. Interdiscip. Top.*, 1996, **54**, 6633.
42 L. Woodcock, *Ann. New York Acad. Sci.*, 1981, **371**, 274.
43 R. W. Style and S. S. L. Peppin, *Proc. R. Soc. London, Ser. A*, 2011, **467**, 174.
44 K. E. Davis and W. B. Russel, *Phys. Fluids A*, 1989, **1**, 82.
45 J. Happel and H. Brenner, *Low Reynolds number hydrodynamics*, Kluwer Academic Publishers, 1991.
46 J.-B. Salmon and J. Leng, *J. Appl. Phys.*, 2010, **107**, 084905.
47 J. Leng, *Phys. Rev. E: Stat., Nonlinear, Soft Matter Phys.*, 2010, **82**, 021405.
48 A. G. Marin, H. Gelderblom, D. Lohse and J. H. Snoeijer, *Phys. Rev. Lett.*, 2011, **107**, 085502.
49 D. Gasperino, L. Meng, D. J. Norris and J. J. Derby, *J. Cryst. Growth*, 2008, **310**, 131.
50 A. Sarkar and M. S. Tirumkudulu, *Langmuir*, 2009, **25**, 4945.
51 I. Nikiforow, J. Adams, A. M. Konig, A. Langhoff, K. Pohl, A. Turshatov and D. Johannsmann, *Langmuir*, 2010, **26**, 13162.
52 B. Abecassis, C. Cottin-Bizonne, C. Ybert, A. Ajdari and L. Bocquet, *Nat. Mater.*, 2008, **7**, 785.
53 L. Belloni, *J. Chem. Phys.*, 2005, **123**, 204705.